

RESEARCH ARTICLE

View Article Online
View Journal | View IssueCite this: *Mater. Chem. Front.*,
2024, 8, 2874

Design of Cr³⁺-activated broadband NIR phosphors with tunable and abnormal thermal quenching behavior for NIR pc-LEDs†

Qijian Zhu,^{‡,ab} Jiansheng Huo,^{‡,a} Quwei Ni,^{ab} Qihong Zhang,^a Junhao Li,^{‡,a} Haiyong Ni^a and Jianbang Zhou^{‡,a*}

Cr³⁺-activated broadband near-infrared (NIR) phosphors usually show controllable and excellent photoluminescence (PL) properties, but their poor thermal stability remains a big challenge. Herein, a series of Lu_{3-x}Ca_xGa_{5-x}Si_xO₁₂:Cr³⁺ garnet phosphors with tunable and abnormal thermal quenching performance have been successfully proposed. It is found that both the crystal field strength and calculated energetic difference between ⁴T₂ and ²E states decrease obviously with increasing [Ca²⁺-Si⁴⁺] co-substitution, resulting in the thermal occupation of the ⁴T₂ state and broadened PL spectra. More importantly, the Lu_{3-x}Ca_xGa_{5-x}Si_xO₁₂:Cr³⁺ phosphors show improved PL thermal stability depending on the different thermal population between ⁴T₂ and ²E states, and the mechanism is investigated in detail. The PL intensity of the optimal sample reaches up to 125% and 121% at 425 K and 475 K compared with that at 300 K, respectively, which is much better than those of most Cr³⁺-activated broadband NIR phosphors. A NIR phosphor-converted light-emitting diode (NIR pc-LED) has been fabricated using the as-prepared thermally stable phosphor and its application in bio-imaging and night vision is demonstrated.

Received 13th May 2024,
Accepted 27th June 2024

DOI: 10.1039/d4qm00395k

rsc.li/frontiers-materials

1. Introduction

Nowadays, NIR spectroscopy is widely used in many fields of our daily life, such as food quality analysis, night vision, medical imaging, plant growth, and so on.¹ Among the various NIR sources, NIR pc-LEDs have received much attention due to the merits of high efficiency, small size, energy saving, environmentally friendly nature and tunable PL properties over the traditional ones (NIR LEDs, tungsten and halogen lamps).^{2,3} As a key component of NIR pc-LEDs, the PL properties of phosphors have a great influence on the performance of LED devices.⁴ It is known that the working temperature of the LED device can reach up to above 100 °C (even 150 °C) because of accumulated heat from the chip.⁵ The PL intensity of NIR phosphors usually decreases obviously due

to enhanced non-radiative transition with increasing temperature,⁶ leading to a decreased device performance. Therefore, the development of NIR phosphors with improved thermal stability is quite important for further applications.⁷

Cr³⁺-activated NIR phosphors usually show strong absorption (⁴A₂ → ⁴T₁) in the blue light region, which can match well with that of the commercial blue LED chip.⁸ In addition, the broadband NIR emission (peak position and bandwidth) of Cr³⁺ can be easily tuned depending on the crystal field strength, due to its unique 3d³ electron configuration.^{4,9} Thanks to the above characteristics, Cr³⁺ is considered to be an ideal NIR emitter and has been extensively explored in recent years. For example, Na₃ScF₆:Cr³⁺ (λ_{em} = 774 nm, FWHM ≈ 108 nm, and I_{425K} ≈ 27%) shows a high Cr³⁺ doping concentration (35.96%) and the internal quantum efficiency (IQE) and external quantum efficiency (EQE) are as high as 91.5% and 40.82%, respectively.¹⁰ Through lithium ion compensation, Mg₄Ta₂O₉:Cr³⁺ (λ_{em} = 842 nm, FWHM ≈ 167 nm, and I_{425K} ≈ 25%) reaches a record EQE of 61.25%.¹¹ Compounds with a garnet structure are popular hosts for Cr³⁺ ions due to the wide bandgap, high structural rigidity and adjustable composition, such as Gd_{2.4}Lu_{0.6}Ga₄AlO₁₂:Cr³⁺ (λ_{em} = 728 nm, FWHM ≈ 107 nm, and I_{425K} ≈ 75%),¹² CaLu₂Mg₂Si₃O₁₂:Cr³⁺ (λ_{em} = 765 nm, FWHM ≈ 120 nm, and I_{425K} ≈ 82%),¹³ and Gd₃Sc₂Ga₃O₁₂:Cr³⁺ (λ_{em} = 760 nm, FWHM ≈ 120 nm, and I_{425K} ≈ 86%).¹⁴ Although the above-mentioned Cr³⁺-activated broadband NIR phosphors show

^a Guangdong Provincial Key Laboratory of Rare Earth Development and Application, Institute of Resources Utilization and Rare Earth Development, Guangdong Academy of Sciences, Guangzhou 510651, P. R. China.
E-mail: zhoujb4079@foxmail.com

^b School of Chemistry, Guangzhou Key Laboratory of Analytical Chemistry for Biomedicine, South China Normal University, Guangzhou 510006, P. R. China

† Electronic supplementary information (ESI) available: The excitation spectra, FWHM, decay curves and temperature-dependent spectra of Lu_{3-x}Ca_xGa_{5-x}Si_xO₁₂:Cr³⁺; XRD patterns, PL intensity, PLE and temperature-dependent spectra of Lu_{2.7}Ca_{0.3}Ga_{4.7-x}Si_{0.3}O₁₂:xCr³⁺ (x = 0.005–0.040); electroluminescence spectrum of the LED device. See DOI: <https://doi.org/10.1039/d4qm00395k>

‡ Q. J. Zhu and J. S. Huo contributed equally to this work.

excellent PL properties and high luminous efficiency, the poor thermal stability still remains a big challenge before practical application, especially for high-power devices.

In this work, a series of $\text{Lu}_{3-x}\text{Ca}_x\text{Ga}_{5-x}\text{Si}_x\text{O}_{12}:\text{Cr}^{3+}$ phosphors with tunable and abnormal thermal quenching performance are designed and presented. It is found that the temperature-dependent luminescence properties of $\text{Lu}_{3-x}\text{Ca}_x\text{Ga}_{5-x}\text{Si}_x\text{O}_{12}:\text{Cr}^{3+}$ can be controlled by the thermal population of the $^4\text{T}_2$ energy level, which is highly related to the energetic difference between $^4\text{T}_2$ and ^2E states.

2. Experimental section

2.1 Synthesis

A series of $\text{Lu}_{3-x}\text{Ca}_x\text{Ga}_{5-x}\text{Si}_x\text{O}_{12}:0.010\text{Cr}^{3+}$ ($x = 0-0.5$) phosphors were synthesized by a traditional high-temperature solid-state reaction method. Lu_2O_3 (99.995%), CaCO_3 (A.R.), SiO_2 (99.95%), Cr_2O_3 (A.R.), Ga_2O_3 (99.99%) and NH_4Cl (A. R.) were used as raw materials without further purification. The raw materials were weighed stoichiometrically (0.3 wt% of NH_4Cl as flux) and finely ground in an agate mortar for 20 min. The mixture was transferred to a corundum crucible and sintered at 1300 °C for 5 h. After cooling to room temperature, the samples were reground for further characterization. $\text{Lu}_{2.7}\text{Ca}_{0.3}\text{Ga}_{4.7-x}\text{Si}_{0.3}\text{O}_{12}:x\text{Cr}^{3+}$ ($x = 0.005-0.040$) phosphors were synthesized similarly according to the above procedures.

2.2 Characterization

The phase purity and crystal structure of the samples were confirmed using a Bruker D8 Advance X-ray diffractometer

(XRD) operating with a Cu K α radiation source ($\lambda = 1.5405 \text{ \AA}$) under 40 kV and 40 mA. Measurements were carried out at room temperature over 5–90° 2θ range. Rietveld refinement was performed using TOPAS-Academic V5 software. The PL excitation (PLE) spectra, PL spectra, and PL decay curves were measured on a FLS1000 spectrometer (Edinburgh Instruments, a 450 W Xe900 continuous xenon lamp as the excitation source) equipped with a thermo-electronic cooled (–22 °C) R928P photomultiplier (PMT) from Hamamatsu and a MercuryITC temperature controller (Oxford).

2.3 LED fabrication

The NIR pc-LED device was fabricated by coating the prepared NIR phosphor on an InGaN blue chip (450 nm, 1 W) with a mass ratio of the phosphor to epoxy resin of 1:1. The current-dependent electroluminescence and output power were collected using an ATA-1000 photoelectric measuring system (EVERFINE, China).

3. Results and discussion

3.1. Crystal structure of $\text{Lu}_{3-x}\text{Ca}_x\text{Ga}_{5-x}\text{Si}_x\text{O}_{12}$

The phase purity of as-prepared $\text{Lu}_{3-x}\text{Ca}_x\text{Ga}_{5-x}\text{Si}_x\text{O}_{12}:\text{Cr}^{3+}$ ($x = 0-0.5$) phosphors was examined by X-ray diffraction (XRD). All the diffraction peaks are in good agreement with the standard data of $\text{Lu}_3\text{Ga}_5\text{O}_{12}$ (PDF no. 13-0400) and no impurity peaks are observed (Fig. 1a), indicating that the co-substitution of $[\text{Lu}^{3+}-\text{Ga}^{3+}]$ by $[\text{Ca}^{2+}-\text{Si}^{4+}]$ has almost no influence on the crystal structure.

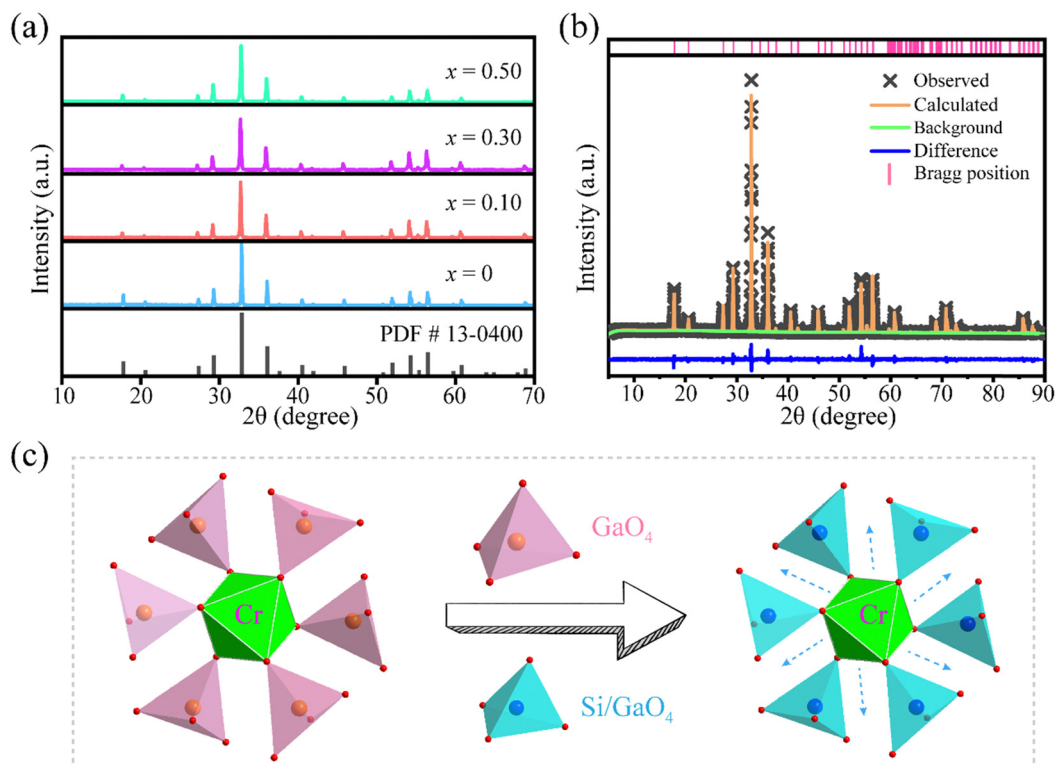


Fig. 1 (a) XRD patterns of $\text{Lu}_{3-x}\text{Ca}_x\text{Ga}_{5-x}\text{Si}_x\text{O}_{12}:\text{Cr}^{3+}$ ($x = 0-0.5$). (b) The Rietveld refinement of $\text{Lu}_{2.7}\text{Ca}_{0.3}\text{Ga}_{4.7}\text{Si}_{0.3}\text{O}_{12}:\text{Cr}^{3+}$ ($R_p = 6.00\%$, $R_{wp} = 10.23\%$). (c) The crystal structure.

The Rietveld refinement (Fig. 1b) is performed using $\text{Lu}_3\text{Ga}_5\text{O}_{12}$ as the starting model, and the small residual factors ($R_p = 6.00\%$, $R_{wp} = 10.23\%$, Table S1, ESI[†]) further confirm the good phase purity. $\text{Lu}_{3-x}\text{Ca}_x\text{Ga}_{5-x}\text{Si}_x\text{O}_{12}$ crystallize in the same space group $Ia\bar{3}d$ (no. 230) as the $\text{Lu}_3\text{Ga}_5\text{O}_{12}$ garnet and there are three kinds of polyhedra in the garnet structure: $(\text{Lu}/\text{Ca})\text{O}_8$ dodecahedra, GaO_6 octahedra and $(\text{Ga}/\text{Si})\text{O}_4$ tetrahedra (Fig. 1c). Cr^{3+} ions ($r = 0.615 \text{ \AA}$, CN = 6) prefer to replace the octahedral Ga^{3+} site ($r = 0.62 \text{ \AA}$, CN = 6) due to the similar radius. The $(\text{Ga}/\text{Cr})\text{O}_6$ octahedra might be enlarged and distorted (Fig. 1c) due to the much smaller ionic radius of Si^{4+} ($r = 0.26 \text{ \AA}$ and CN = 4) than Ga^{3+} ($r = 0.47 \text{ \AA}$ and CN = 4), indicating a weakening crystal field strength,¹⁵ and then a broadened emission can be anticipated with increasing x values in $\text{Lu}_{3-x}\text{Ca}_x\text{Ga}_{5-x}\text{Si}_x\text{O}_{12}:\text{Cr}^{3+}$ phosphors.

Fig. S1 (ESI[†]) presents the SEM and elemental mapping images of $\text{Lu}_{2.7}\text{Ca}_{0.3}\text{Ga}_{4.7}\text{Si}_{0.3}\text{O}_{12}:\text{Cr}^{3+}$ phosphors, which show an irregular shape with several hundred nanometers in size. All the elements such as Lu, Ga, Ca, Si, O and Cr are found to be distributed uniformly in the matrix.

3.2. PL properties of $\text{Lu}_{3-x}\text{Ca}_x\text{Ga}_{5-x}\text{Si}_x\text{O}_{12}:\text{Cr}^{3+}$

To investigate the influence of $[\text{Ca}^{2+}-\text{Si}^{4+}]$ co-substitution on the PL properties, the emission spectra of $\text{Lu}_{3-x}\text{Ca}_x\text{Ga}_{5-x}\text{Si}_x\text{O}_{12}:\text{Cr}^{3+}$ are studied in detail. It can be seen that the room-temperature PL spectrum of $\text{Lu}_3\text{Ga}_5\text{O}_{12}:\text{Cr}^{3+}$ is dominated by a sharp emission peaked at 705 (R_1 line) and 691 nm (R_2 line) corresponding to

${}^2\text{E} \rightarrow {}^4\text{A}_2$ transition of Cr^{3+} (Fig. 2a). Meanwhile, the broadband emission from 620 to 830 nm comes from ${}^4\text{T}_2 \rightarrow {}^4\text{A}_2$ transition.¹⁶ With increasing $[\text{Ca}^{2+}-\text{Si}^{4+}]$ co-substitution, the PL intensity of the broadband ${}^4\text{T}_2 \rightarrow {}^4\text{A}_2$ emission increases significantly (Fig. 2b), leading to an increased value (from 43 to 150 nm, Fig. S2, ESI[†]) of full width at half maximum (FWHM).

The spectral broadening of $\text{Lu}_{3-x}\text{Ca}_x\text{Ga}_{5-x}\text{Si}_x\text{O}_{12}:\text{Cr}^{3+}$ is probably related to the decrease of crystal field strength with x value. As is well known, the energy of the ${}^4\text{T}_2$ level of Cr^{3+} is lower than that of the ${}^2\text{E}$ level when exposed to a weak crystal field, according to the Tanabe–Sugano diagram for the $3d^3$ electron configuration (Fig. 2c), and the PL spectra consist of an intense broadband emission band. The energy of the ${}^2\text{E}$ level is lower as a result of a strong crystal field, and the PL spectra consist of a sharp emission line. When Cr^{3+} ions are exposed to intermediate crystal fields, both emission bands are visible in the PL spectra. Therefore, to further explore the influence of $[\text{Ca}^{2+}-\text{Si}^{4+}]$ co-substitution on the PL properties, the crystal field splitting parameters (Dq and B) of $\text{Lu}_{3-x}\text{Ca}_x\text{Ga}_{5-x}\text{Si}_x\text{O}_{12}:\text{Cr}^{3+}$ ($x = 0-0.5$) are calculated from the PL excitation spectra (PLE, Fig. S3, ESI[†]) with the following equations:^{17,18}

$$10Dq = E({}^4\text{T}_2) = E({}^4\text{A}_2 \rightarrow {}^4\text{T}_2) \quad (1)$$

$$\frac{Dq}{B} = \frac{15(\Delta E/Dq - 8)}{(\Delta E/Dq)^2 - 10(\Delta E/Dq)} \quad (2)$$

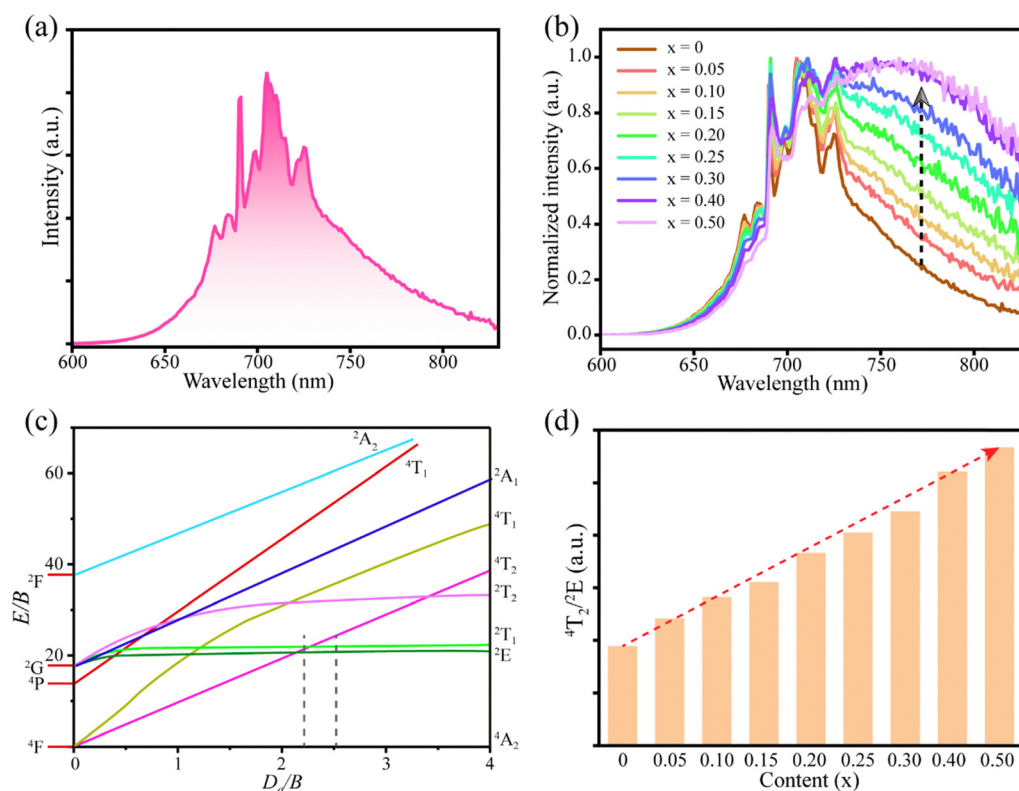


Fig. 2 (a) Emission spectrum of $\text{Lu}_3\text{Ga}_5\text{O}_{12}:\text{Cr}^{3+}$ ($\lambda_{\text{ex}} = 430 \text{ nm}$). (b) Emission spectra ($\lambda_{\text{ex}} = 430 \text{ nm}$) of $\text{Lu}_{3-x}\text{Ca}_x\text{Ga}_{5-x}\text{Si}_x\text{O}_{12}:\text{Cr}^{3+}$ ($x = 0-0.5$). (c) Tanabe–Sugano diagram of Cr^{3+} ions in an octahedral coordination. (d) Fluorescence intensity ratio (FIR) of ${}^4\text{T}_2 \rightarrow {}^4\text{A}_2$ to ${}^2\text{E} \rightarrow {}^4\text{A}_2$ [$I({}^4\text{T}_2)/I({}^2\text{E})$] transitions of $\text{Lu}_{3-x}\text{Ca}_x\text{Ga}_{5-x}\text{Si}_x\text{O}_{12}:\text{Cr}^{3+}$ ($x = 0-0.5$).

Table 1 Crystal field splitting parameter Dq , Racah parameter B and values of energy levels of $\text{Lu}_{3-x}\text{Ca}_x\text{Ga}_{4.99-x}\text{Si}_x\text{O}_{12}:0.01\text{Cr}^{3+}$ ($x = 0-0.5$)

x	Dq (cm^{-1})	B (cm^{-1})	Dq/B	Δ_1 (cm^{-1})	$S\hbar\omega$ (cm^{-1})	Δ_2 (cm^{-1})
0	1652.89	655.07	2.52	2344.53	1551.25	793.28
0.05	1639.34	667.91	2.45	2209.05	1592.36	616.69
0.1	1631.32	680.03	2.40	2148.91	1648.02	500.89
0.15	1626.02	680.84	2.39	2115.89	1674.10	441.79
0.2	1623.38	684.91	2.37	2109.47	1709.93	399.54
0.25	1618.12	685.71	2.36	2116.53	1742.04	374.49
0.3	1612.90	693.89	2.32	2064.33	1749.85	314.48
0.4	1602.56	702.92	2.28	1960.94	1733.48	227.46
0.5	1594.90	715.45	2.23	1923.72	1706.64	217.08

$$\Delta E = E(^4T_1) - E(^4T_2) = E(^4A_2 \rightarrow ^4T_1) - E(^4A_2 \rightarrow ^4T_2) \quad (3)$$

Here, Dq and B represent the crystal field strength and repulsive force between 3d electrons, respectively.¹⁶ The calculated results are shown in Table 1. It can be seen that the Dq/B values of $\text{Lu}_{3-x}\text{Ca}_x\text{Ga}_{4.99-x}\text{Si}_x\text{O}_{12}:\text{Cr}^{3+}$ decrease from 2.52 to 2.23 with increasing x , indicating that a decreased crystal field strength is obtained with increasing $[\text{Ca}^{2+}-\text{Si}^{4+}]$ co-substitution. The weakened crystal field strength downshifts the 4T_2 energy level (Fig. 2c), due to which the possibility of thermal population at the 4T_2 state will increase compared with that at the 2E state,¹⁵ leading to an increased fluorescence intensity ratio (FIR) of $^4T_2 \rightarrow ^4A_2$ to $^2E \rightarrow ^4A_2$ [$I(^4T_2)/I(^2E)$] transitions (Fig. 2d). The decreased lifetime of $\text{Lu}_{3-x}\text{Ca}_x\text{Ga}_{4.99-x}\text{Si}_x\text{O}_{12}:0.01\text{Cr}^{3+}$ (Fig. S4, ESI[†]) is another evidence for the thermally populated 4T_2 energy level.¹⁹

To further analyze the PL properties of $\text{Lu}_{3-x}\text{Ca}_x\text{Ga}_{4.99-x}\text{Si}_x\text{O}_{12}:0.01\text{Cr}^{3+}$ in detail, a configurational coordinate diagram

(Fig. 3a) is constructed based on the obtained spectral characteristics. Δ_1 is the energetic difference between the R_1 line and the maximum of the $^4A_2 \rightarrow ^4T_2$ PLE band.²⁰ The energetic difference Δ_2 between 4T_2 and 2E electronic manifolds, which determines the thermal occupation of the 4T_2 energy level, can be obtained from the following relationship:^{21,22}

$$\Delta_2 = \Delta_1 - S\hbar\omega \quad (4)$$

where S and $\hbar\omega$ are the Huang-Rhys factor and effective phonon energy, respectively. The values of S and $\hbar\omega$ can be calculated using the following equations:²³

$$\Delta E = (2S - 1)\hbar\omega \quad (5)$$

$$\Gamma(T) = 2.35\hbar\omega \sqrt{S \coth\left(\frac{\hbar\omega}{2kT}\right)} \quad (6)$$

where ΔE is the Stokes shift (energy difference between the first absorption and corresponding emission bands) and $\Gamma(T)$ is the FWHM of the emission band at temperature T . The Δ_2 values of $\text{Lu}_{3-x}\text{Ca}_x\text{Ga}_{4.99-x}\text{Si}_x\text{O}_{12}:0.01\text{Cr}^{3+}$ are calculated according to the above equations and the results are shown in Fig. 3b. It can be seen that the values of Δ_2 decrease with increasing x , indicating a higher probability of $^2E \rightarrow ^4T_2$ transition (*i.e.* thermally populated 4T_2 state) which is consistent with the enhanced $^4T_2 \rightarrow ^4A_2$ broadband emission and increased FIR of $I(^4T_2)/I(^2E)$ of $\text{Lu}_{3-x}\text{Ca}_x\text{Ga}_{4.99-x}\text{Si}_x\text{O}_{12}:0.01\text{Cr}^{3+}$ (as shown in Fig. 2b and d).

3.3. Thermal stability of $\text{Lu}_{3-x}\text{Ca}_x\text{Ga}_{4.99-x}\text{Si}_x\text{O}_{12}:\text{Cr}^{3+}$

The PL intensity of phosphors usually shows a decreasing trend due to enhanced non-radiative transition with increasing temperature, which is a major obstacle for their application. Therefore, it is of great importance to develop NIR phosphors with improved thermal stability. In previous work,²⁴ it is verified that the PL thermal stability of Cr^{3+} can be optimized by the electron occupation between 4T_2 and 2E states. As discussed above, the energetic difference Δ_2 and crystal field strength (Table 1) between 4T_2 and 2E states (thermal population of the 4T_2 state) of $\text{Lu}_{3-x}\text{Ca}_x\text{Ga}_{4.99-x}\text{Si}_x\text{O}_{12}:0.01\text{Cr}^{3+}$ can be easily tuned by co-substitution of $[\text{Lu}^{3+}-\text{Ga}^{3+}]$ by $[\text{Ca}^{2+}-\text{Si}^{4+}]$, which may provide an alternative way for improving the thermal stability.

In order to evaluate the influence of $[\text{Ca}^{2+}-\text{Si}^{4+}]$ co-substitution on thermal stability, the temperature-dependent PL spectra of $\text{Lu}_{3-x}\text{Ca}_x\text{Ga}_{4.99-x}\text{Si}_x\text{O}_{12}:0.01\text{Cr}^{3+}$ ($x = 0, 0.15$ and 0.30) are studied in detail (Fig. 4 and Fig. S5, ESI[†]). On the one hand, it is noted that the integrated PL intensity of all $\text{Lu}_{3-x}\text{Ca}_x\text{Ga}_{4.99-x}\text{Si}_x\text{O}_{12}:0.01\text{Cr}^{3+}$ ($x = 0, 0.15$ and 0.30) samples increases first and then decreases with increasing temperature (Fig. 4a-c). On the other hand, the thermal stability of $\text{Lu}_{3-x}\text{Ca}_x\text{Ga}_{4.99-x}\text{Si}_x\text{O}_{12}:0.01\text{Cr}^{3+}$ becomes better and better with increasing x and the PL intensity at $x = 0.30$ reaches up to 125% and 121% at 425 K and 475 K compared with that at 300 K (Fig. 4c), respectively, which is much better than those of most Cr^{3+} -activated broadband NIR phosphors (Table 2).

To understand the mechanism behind the abnormal thermal stability, the PL spectra are deconvoluted into separate $^4T_2 \rightarrow ^4A_2$ broadband and $^2E \rightarrow ^4A_2$ sharp-line emissions for all

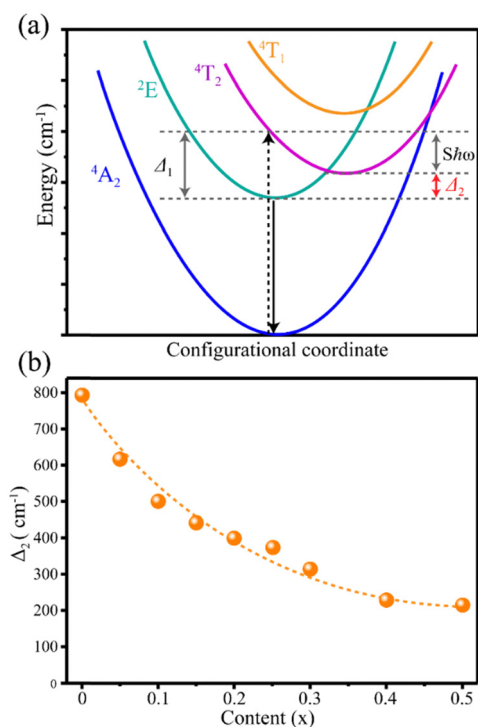


Fig. 3 (a) Schematic configurational coordinate diagram and (b) energy difference between 4T_2 and 2E states of $\text{Lu}_{3-x}\text{Ca}_x\text{Ga}_{4.99-x}\text{Si}_x\text{O}_{12}:0.01\text{Cr}^{3+}$ ($x = 0-0.5$).

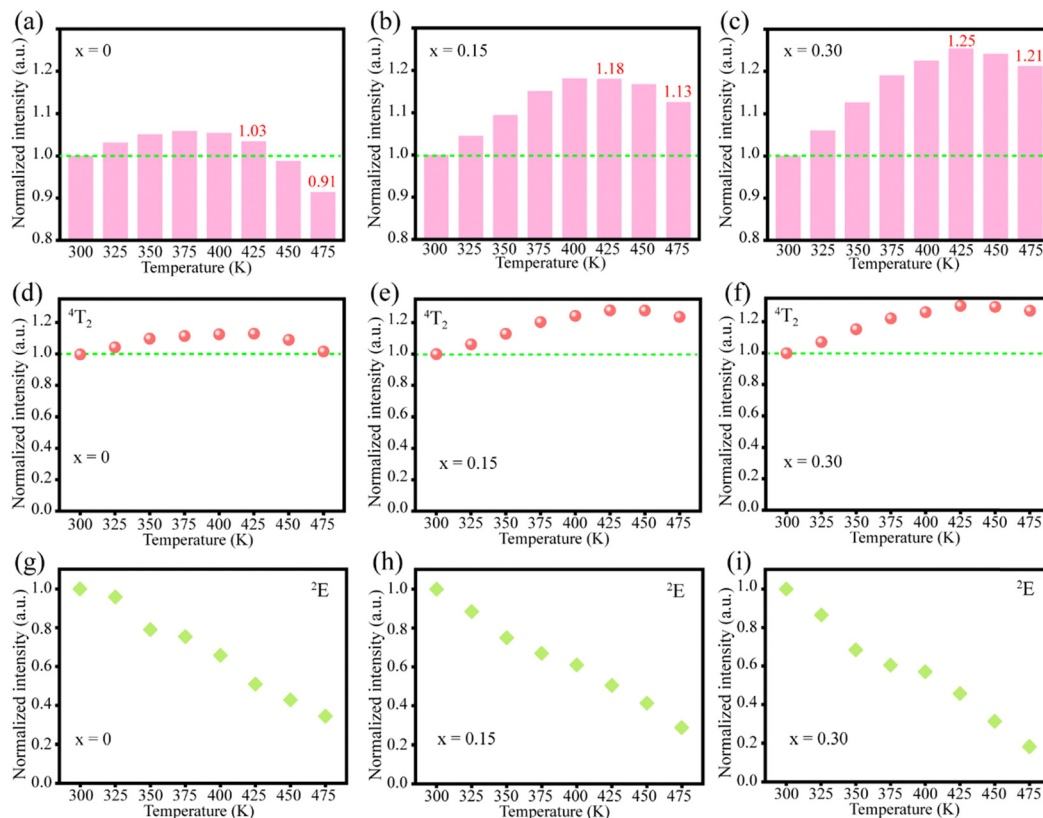


Fig. 4 Normalized PL intensity of (a)–(c) ${}^4T_2 + {}^2E \rightarrow {}^4A_2$, (d)–(f) ${}^4T_2 \rightarrow {}^4A_2$ and (g)–(i) ${}^2E \rightarrow {}^4A_2$ transitions of $\text{Lu}_{3-x}\text{Ca}_x\text{Ga}_{5-x}\text{Si}_x\text{O}_{12}:0.01\text{Cr}^{3+}$ as a function of temperature (300–475 K) with $x = 0, 0.15$ and 0.30 , respectively.

temperatures.²² The PL intensity of the ${}^4T_2 \rightarrow {}^4A_2$ broadband emission (Fig. 4d–f) exhibits a similar trend to the corresponding total PL intensity (Fig. 4a–c), while the ${}^2E \rightarrow {}^4A_2$ sharp-line emission (Fig. 4g–i) decreases monotonically with x . In the $\text{Lu}_{3-x}\text{Ca}_x\text{Ga}_{5-x}\text{Si}_x\text{O}_{12}$ system, the 2E state can serve as a reservoir for the higher lying 4T_2 state.¹⁹ The electrons will migrate from the 2E to 4T_2 energy level with increasing temperature and reach a new thermal equilibrium, leading to a thermally populated 4T_2 state (which can be further verified by the decay curves in Fig. S6, ESI†). This explains why $\text{Lu}_{3-x}\text{Ca}_x\text{Ga}_{5-x}\text{Si}_x\text{O}_{12}:0.01\text{Cr}^{3+}$ phosphors exhibit an abnormal thermal stability before 425 K. At higher temperatures, the ${}^4T_2 \rightarrow {}^4A_2$ broadband emission dominates the PL spectra and then a

traditional thermal quenching phenomenon is observed due to the increased non-radiative rate of the 4T_2 level.

The improved thermal stability of $\text{Lu}_{3-x}\text{Ca}_x\text{Ga}_{5-x}\text{Si}_x\text{O}_{12}:0.01\text{Cr}^{3+}$ ($x = 0, 0.15$ and 0.30) with increasing x is due to the different energetic difference Δ_2 between 4T_2 and 2E states which has a great influence on the initial thermal equilibrium between 4T_2 and 2E energy levels (*i.e.* FIR of $I({}^4T_2)/I({}^2E)$) and determines the thermal quenching performance at elevated temperatures. The PL intensity of ${}^2E \rightarrow {}^4A_2$ sharp-line emission is strong at large Δ_2 values (small x), whose decrease has a great influence on the whole PL intensity with increasing temperature. Then the ${}^2E \rightarrow {}^4T_2$ transition strengthens with decreasing Δ_2 (increasing x). Finally, the ${}^2E \rightarrow {}^4T_2$ transition has little influence on the thermal quenching performance due to the insufficient 2E electrons for smaller Δ_2 values. That is why the thermal stability of $\text{Lu}_{3-x}\text{Ca}_x\text{Ga}_{5-x}\text{Si}_x\text{O}_{12}:0.01\text{Cr}^{3+}$ decreases when $x > 0.30$ (Fig. S7, ESI†). In this work, it is obvious that $\text{Lu}_{3-x}\text{Ca}_x\text{Ga}_{5-x}\text{Si}_x\text{O}_{12}:0.01\text{Cr}^{3+}$ phosphors have optimal Δ_2 values and the best thermal stability when $x = 0.30$.

Considering the higher thermal stability (Fig. 3c) and PL intensity (Fig. S8, ESI†) of $\text{Lu}_{3-x}\text{Ca}_x\text{Ga}_{5-x}\text{Si}_x\text{O}_{12}:0.01\text{Cr}^{3+}$ at $x = 0.30$, a series of $\text{Lu}_{2.7}\text{Ca}_{0.3}\text{Ga}_{4.7}\text{Si}_{0.3}\text{O}_{12}:\text{Cr}^{3+}$ with various Cr^{3+} concentrations were prepared (Fig. S9, ESI†) to further optimize the PL properties (Fig. 5a). The PL intensity of $\text{Lu}_{2.7}\text{Ca}_{0.3}\text{Ga}_{4.7-x}\text{Si}_{0.3}\text{O}_{12}:\text{Cr}^{3+}$ reaches its maximum value at $x = 0.02$ (Fig. S10, ESI†) and then decreases owing to the concentration

Table 2 Thermal stability of Cr^{3+} -activated broadband NIR phosphors

Phosphors	λ_{em} (nm)	$I_{423\text{K}}$ (%)	Ref.
$\text{Lu}_{2.7}\text{Ca}_{0.3}\text{Ga}_{4.7}\text{Si}_{0.3}\text{O}_{12}:\text{Cr}^{3+}$	748	125	This work
$\text{Y}_3\text{In}_2\text{Ga}_3\text{O}_{12}:\text{Cr}^{3+}$	760	100	25
$\text{Ca}_3\text{Sc}_2\text{Si}_3\text{O}_{12}:\text{Cr}^{3+}$	770	97.4	26
$\text{GaTaO}_4:\text{Cr}^{3+}$	840	60	27
$\text{ScBO}_3:\text{Cr}^{3+}$	800	51	28
$\text{Na}_3\text{Al}_2\text{Li}_3\text{F}_{12}:\text{Cr}^{3+}$	750	99	29
$\text{K}_2\text{NaInF}_6:\text{Cr}^{3+}$	774	78.3	30
$\text{K}_2\text{NaScF}_6:\text{Cr}^{3+}$	765	89.6	31
$\text{ScF}_3:\text{Cr}^{3+}$	853	85.5	32

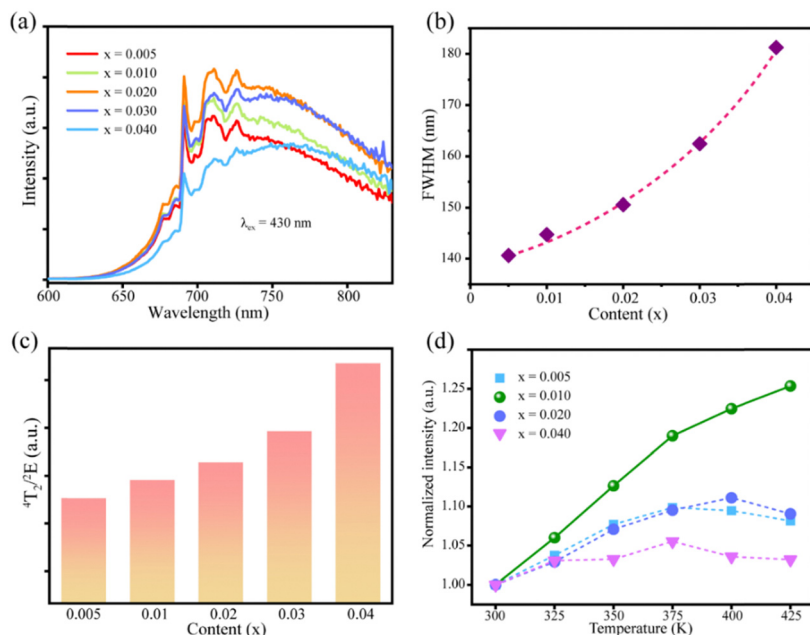


Fig. 5 (a) Emission spectra, (b) FWHM and (c) FIR of 4T_2 4A_2 to ${}^2E \rightarrow {}^4A_2$ transitions of $\text{Lu}_{2.7}\text{Ca}_{0.3}\text{Ga}_{4.7-x}\text{Si}_{0.3}\text{O}_{12}:\text{xCr}^{3+}$ ($x = 0.005$ – 0.040). (d) Normalized PL intensity of $\text{Lu}_{2.7}\text{Ca}_{0.3}\text{Ga}_{4.7-x}\text{Si}_{0.3}\text{O}_{12}:\text{xCr}^{3+}$ as a function of temperature (300–425 K).

quenching effect. Moreover, it is found that both the FWHM (from 140 to 182 nm, Fig. 5b) and FIR (Fig. 5c) of $I({}^4T_2)/I({}^2E)$ show an increasing trend as the Cr^{3+} concentration increases, just like that of $\text{Lu}_{3-x}\text{Ca}_x\text{Ga}_{5-x}\text{Si}_x\text{O}_{12}:0.01\text{Cr}^{3+}$ (Fig. 2b, d). But the reason for the increased ${}^4T_2 \rightarrow {}^4A_2$ broadband emission with increasing Cr^{3+} content is different from that of $\text{Lu}_{3-x}\text{Ca}_x\text{Ga}_{5-x}\text{Si}_x\text{O}_{12}:0.01\text{Cr}^{3+}$

(which is due to a decreased crystal field strength). In this case, the normalized PLE spectra of $\text{Lu}_{2.7}\text{Ca}_{0.3}\text{Ga}_{4.7-x}\text{Si}_{0.3}\text{O}_{12}:\text{xCr}^{3+}$ almost overlap with each other (Fig. S11 (ESI⁺), implying an unchanged crystal field strength). It is considered that the distance between Cr^{3+} and Cr^{3+} ions in $\text{Lu}_{2.7}\text{Ca}_{0.3}\text{Ga}_{4.7-x}\text{Si}_{0.3}\text{O}_{12}:\text{xCr}^{3+}$ decreases with increasing Cr^{3+} concentration, which is conducive

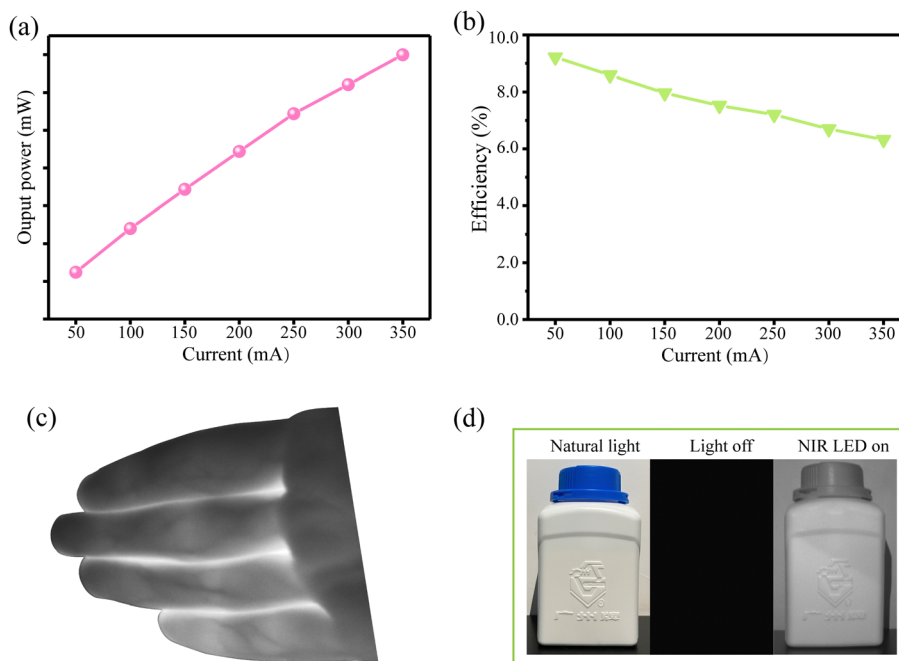


Fig. 6 (a) Output power and (b) photoelectric conversion efficiency of the fabricated NIR-LED device as a function of driven current. (c) Photograph of fingers taken with the NIR camera under irradiation of the LED device. (d) Photographs of a bottle under natural light and NIR LED light captured with a visible camera (left and middle) and the NIR camera (right).

to the electron migration from the 2E to 4T_2 state, thus resulting in a thermally populated 4T_2 state (*i.e.* enhanced ${}^4T_2 \rightarrow {}^4A_2$ broadband emission) at higher Cr^{3+} content.²⁴

Due to the varying FIR values of $I({}^4T_2)/I({}^2E)$ of $Lu_{2.7}Ca_{0.3}Ga_{4.7-x}Si_{0.3}O_{12}:xCr^{3+}$, it is necessary to investigate the thermal stability. The temperature-dependent PL spectra of $Lu_{2.7}Ca_{0.3}Ga_{4.7-x}Si_{0.3}O_{12}:xCr^{3+}$ are measured and shown in Fig. 5d and Fig. S12 (ESI[†]). As expected, the thermal stability of $Lu_{2.7}Ca_{0.3}Ga_{4.7-x}Si_{0.3}O_{12}:xCr^{3+}$ becomes better before $x = 0.010$ and then decreases due to the gradually exhausting 2E electrons at higher Cr^{3+} concentration. From the obtained results, it can be inferred that both the Δ_2 value and Cr^{3+} concentration have a significant influence on the thermal stability of $Lu_{3-x}Ca_xGa_{5-x}Si_xO_{12}:Cr^{3+}$.

3.4. NIR pc-LED applications

Considering the excellent thermal quenching behavior of the as-prepared samples, a NIR pc-LED was fabricated by combining a $Lu_{2.7}Ca_{0.3}Ga_{4.7}Si_{0.3}O_{12}:Cr^{3+}$ phosphor with a commercial blue InGaN chip and the electroluminescence spectrum is shown in Fig. S13 (ESI[†]). The NIR output power (Fig. 6a) increases monotonously from 50 to 350 mA, while the photoelectric conversion efficiency decreases slightly (Fig. 6b). The NIR light from the LED device can penetrate human fingers easily and the blood vessels can be observed clearly (Fig. 6c). In addition, with the aid of a NIR camera, the words on the bottle surface are clearly distinguished by using the packaged NIR pc-LED as the light source (Fig. 6d). The above results indicate that the as-prepared sample can be potentially used in the fields of bio-imaging and night vision.

4. Conclusions

In summary, $Lu_{3-x}Ca_xGa_{5-x}Si_xO_{12}:Cr^{3+}$ phosphors with tunable PL properties and abnormal thermal stability were synthesized by a high-temperature solid-state method. The FWHM of the PL spectra of $Lu_{3-x}Ca_xGa_{5-x}Si_xO_{12}:Cr^{3+}$ broadens from 43 to 150 nm due to the enhanced ${}^4T_2 \rightarrow {}^4A_2$ emission, resulting from a decreased crystal field strength. The calculated energetic difference (Δ_2) between 4T_2 and 2E states also shows a decreasing trend with increasing $[Ca^{2+}-Si^{4+}]$ co-substitution, leading to a thermally populated 4T_2 state. Based on the different thermal population of the 4T_2 state, the thermal stability of $Lu_{3-x}Ca_xGa_{5-x}Si_xO_{12}:Cr^{3+}$ can be easily tuned. With the optimal $[Ca^{2+}-Si^{4+}]$ co-substitution, $Lu_{3-x}Ca_xGa_{5-x}Si_xO_{12}:0.01Cr^{3+}$ ($x = 0.30$) shows an abnormal thermal quenching performance and the PL intensity can reach up to 125% and 121% at 425 K and 475 K compared with that at 300 K, respectively. In addition, it is found that the ${}^4T_2/{}^2E$ thermal population and PL thermal stability of Cr^{3+} can be further optimized by the Cr^{3+} concentration. Finally, a NIR pc-LED based on the $Lu_{3-x}Ca_xGa_{5-x}Si_xO_{12}:Cr^{3+}$ phosphor shows excellent performance in bio-imaging and night vision.

Data availability

The data supporting this article have been included as part of the ESI.[†]

Conflicts of interest

There are no conflicts to declare.

Acknowledgements

This work has been financially supported by the National Natural Science Foundation of China (No. 52272143), the Major Science and Technology Project of Zhongshan City (No. 2022A1007), the Guangdong Basic and Applied Basic Research Foundation (No. 2023A1515010866 and 2021A1515110404), the Science and Technology Project of Guangzhou City (No. 2023A04J0299), the GDAS' Project of Science and Technology Development (No. 2022GDASZH-2022010104, 2023GDASZH-2023010104 and 2024GDASZH-2024010102), and Young Talent Project of GDAS (No. 2023GDASQNR-0302).

Notes and references

- R.-J. Xie, Light-emitting diodes: brighter NIR-emitting phosphor making light sources smarter, *Light: Sci. Appl.*, 2020, **9**, 155.
- M. H. Fang, Z. Bao, W. T. Huang and R. S. Liu, Evolutionary generation of phosphor materials and their progress in future applications for light-emitting diodes, *Chem. Rev.*, 2022, **122**, 11474–11513.
- G. N. A. De Guzman, M.-H. Fang, C.-H. Liang, Z. Bao, S.-F. Hu and R.-S. Liu, [INVITED] Near-infrared phosphors and their full potential: a review on practical applications and future perspectives, *J. Lumin.*, 2020, **219**, 116944.
- M. H. Fang, K. C. Chen, N. Majewska, T. Lesniewski, S. Mahlik, G. Leniec, S. M. Kaczmarek, C. W. Yang, K. M. Lu, H. S. Sheu and R. S. Liu, Hidden structural evolution and bond valence control in near-infrared phosphors for light-emitting diodes, *ACS Energy Lett.*, 2021, **6**, 109–114.
- J. Feng, H. Liu, Z. Ma, J. Feng, L. Chen, J. Li, Y. Cai, Q. Zeng, D. Wen and Y. Guo, A super stable near-infrared garnet phosphor resistant to thermal quenching, thermal degradation and hydrolysis, *Chem. Eng. J.*, 2022, **449**, 137892.
- G. Liu and Z. Xia, Modulation of thermally stable photoluminescence in Cr^{3+} -based near-infrared phosphors, *J. Phys. Chem. Lett.*, 2022, **13**, 5001–5008.
- J. M. Xiang, J. M. Zheng, X. Q. Zhao, X. Zhou, C. H. Chen, M. K. Jin and C. F. Guo, Synthesis of broadband NIR garnet phosphor $Ca_4ZrGe_3O_{12}:Cr^{3+}, Yb^{3+}$ for NIR pc-LED applications, *Mater. Chem. Front.*, 2022, **6**, 440–449.
- H. Xiao, J. Zhang, L. Zhang, H. Wu, H. Wu, G. Pan, F. Liu and J. Zhang, Cr^{3+} activated garnet phosphor with efficient blue to far-red conversion for pc-LED, *Adv. Opt. Mater.*, 2021, **9**, 2101134.
- J. Zhong, Y. Zhuo, F. Du, H. Zhang, W. Zhao and J. Brgoch, Efficient and tunable luminescence in $Ga_{2-x}In_xO_3:Cr^{3+}$ for near-infrared imaging, *ACS Appl. Mater. Interfaces*, 2021, **13**, 31835–31842.

- 10 F. He, E. Song, Y. Zhou, H. Ming, Z. Chen, J. Wu, P. Shao, X. Yang, Z. Xia and Q. Zhang, A general ammonium salt assisted synthesis strategy for Cr³⁺-doped hexafluorides with highly efficient near infrared emissions, *Adv. Funct. Mater.*, 2021, **31**, 2103743.
- 11 S. Wang, R. Pang, T. Tan, H. Wu, Q. Wang, C. Li, S. Zhang, T. Tan, H. You and H. Zhang, Achieving high quantum efficiency broadband NIR Mg₄Ta₂O₉:Cr³⁺ phosphor through lithium-ion compensation, *Adv. Mater.*, 2023, **35**, 2300124.
- 12 X. Zou, X. Wang, H. Zhang, Y. Kang, X. Yang, X. Zhang, M. S. Molokeev and B. Lei, A highly efficient and suitable spectral profile Cr³⁺-doped garnet near-infrared emitting phosphor for regulating photomorphogenesis of plants, *Chem. Eng. J.*, 2022, **428**, 132003.
- 13 R. Li, Y. Liu, C. Yuan, G. Leniec, L. Miao, P. Sun, Z. Liu, Z. Luo, R. Dong and J. Jiang, Thermally stable CaLu₂Mg₂Si₃O₁₂:Cr³⁺ phosphors for NIR LEDs, *Adv. Opt. Mater.*, 2021, **9**, 2100388.
- 14 E. T. Basore, W. Xiao, X. Liu, J. Wu and J. Qiu, Broadband near-infrared garnet phosphors with near-unity internal quantum efficiency, *Adv. Opt. Mater.*, 2020, **8**, 2000296.
- 15 M. Mao, T. Zhou, H. Zeng, L. Wang, F. Huang, X. Tang and R.-J. Xie, Broadband near-infrared (NIR) emission realized by the crystal-field engineering of Y_{3-x}CaxAl_{5-x}Si₆O₁₂:Cr³⁺ (x = 0-2.0) garnet phosphors, *J. Mater. Chem. C*, 2020, **8**, 1981-1988.
- 16 F. Chi, W. Dai, L. Qiu, S. Liu, X. Wei, Y. Chen and M. Yin, Photoluminescence properties of far-red emitting Lu₂CaAl₄GeO₁₂:Cr³⁺ garnet phosphor, *J. Lumin.*, 2022, **251**, 119198.
- 17 H. J. Yu, J. Chen, R. Y. Mi, J. Y. Yang and Y. G. Liu, Broadband near-infrared emission of K3ScF6:Cr³⁺ phosphors for night vision imaging system sources, *Chem. Eng. J.*, 2021, **417**, 129271.
- 18 J. M. Xiang, X. Zhou, X. Q. Zhao, Z. Y. Wu, C. H. Chen, X. J. Zhou and C. F. Guo, Ab Initio site-selective occupancy and luminescence enhancement in broadband nir emitting phosphor Mg₇Ga₂GeO₁₂:Cr³⁺, *Laser Photonics Rev.*, 2023, **17**, 2200965.
- 19 B. Malysa, A. Meijerink and T. Jüstel, Temperature dependent luminescence Cr³⁺-doped GdAl₃(BO₃)₄ and YAl₃(BO₃)₄, *J. Lumin.*, 2016, **171**, 246-253.
- 20 M.-H. Fang, G. N. A. De Guzman, Z. Bao, N. Majewska, S. Mahlik, M. Grinberg, G. Leniec, S. M. Kaczmarek, C.-W. Yang, K.-M. Lu, H.-S. Sheu, S.-F. Hu and R.-S. Liu, Ultra-high-efficiency near-infrared Ga₂O₃:Cr³⁺ phosphor and controlling of phytochrome, *J. Mater. Chem. C*, 2020, **8**, 11013-11017.
- 21 M. Back, J. Ueda, M. G. Brik, T. Lesniewski, M. Grinberg and S. Tanabe, Revisiting Cr³⁺-doped Bi₂Ga₄O₉ spectroscopy: crystal field effect and optical thermometric behavior of near-infrared-emitting singly-activated phosphors, *ACS Appl. Mater. Interfaces*, 2018, **10**, 41512-41524.
- 22 M.-H. Fang, T.-Y. Li, W.-T. Huang, C.-L. Cheng, Z. Bao, N. Majewska, S. Mahlik, C.-W. Yang, K.-M. Lu, G. Leniec, S. M. Kaczmarek, H.-S. Sheu and R.-S. Liu, Surface-protected high-efficiency nanophosphors via space-limited ship-in-a-bottle synthesis for broadband near-infrared mini-light-emitting diodes, *ACS Energy Lett.*, 2021, **6**, 659-664.
- 23 M. G. Brik and N. M. Avram, Crystal Field Analysis and electron-phonon coupling in Sc₂O₃:Cr³⁺, *Z. Naturforsch., A: Phys. Sci.*, 2014, **56**, 799-803.
- 24 Q. Zhang, X. Wei, J. Zhou, B. Milićević, L. Lin, J. Huo, J. Li, H. Ni and Z. Xia, Thermal stability improvement of Cr³⁺-activated broadband near-infrared phosphors via state population optimization, *Adv. Opt. Mater.*, 2023, **11**, 2300310.
- 25 C. Li and J. Zhong, Highly efficient broadband near-infrared luminescence with zero-thermal-quenching in garnet Y₃In₂Ga₃O₁₂:Cr³⁺ phosphors, *Chem. Mater.*, 2022, **34**, 8418-8426.
- 26 Z. Jia, C. Yuan, Y. Liu, X.-J. Wang, P. Sun, L. Wang, H. Jiang and J. Jiang, Strategies to approach high performance in Cr³⁺-doped phosphors for high-power NIR-LED light sources, *Light: Sci. Appl.*, 2020, **9**, 86.
- 27 J. Y. Zhong, Y. Zhuo, F. Du, H. S. Zhang, W. R. Zhao, S. H. You and J. Brgoch, Efficient broadband near-infrared emission in the GaTaO₄:Cr³⁺ phosphor, *Adv. Opt. Mater.*, 2022, **10**, 2101800.
- 28 M.-H. Fang, P.-Y. Huang, Z. Bao, N. Majewska, T. Leśniewski, S. Mahlik, M. Grinberg, G. Leniec, S. M. Kaczmarek, C.-W. Yang, K.-M. Lu, H.-S. Sheu and R.-S. Liu, Penetrating biological tissue using light-emitting diodes with a highly efficient near-infrared ScBO₃:Cr³⁺ phosphor, *Chem. Mater.*, 2020, **32**, 2166-2171.
- 29 D. Huang, S. Liang, D. Chen, J. Hu, K. Xu and H. Zhu, An efficient garnet-structured Na₃Al₂Li₃F₁₂:Cr³⁺ phosphor with excellent photoluminescence thermal stability for near-infrared LEDs, *Chem. Eng. J.*, 2021, **426**, 131332.
- 30 Z. Wu, X. Han, Y. Zhou, K. Xing, S. Cao, L. Chen, R. Zeng, J. Zhao and B. Zou, Efficient broadband near-infrared luminescence of Cr³⁺ doped fluoride K₂NaInF₆ and its NIR-LED application toward veins imaging, *Chem. Eng. J.*, 2022, **427**, 131740.
- 31 E. Song, H. Ming, Y. Zhou, F. He, J. Wu, Z. Xia and Q. Zhang, Cr³⁺-Doped Sc-Based fluoride enabling highly efficient near infrared luminescence: a case study of K₂NaScF₆:Cr³⁺, *Laser Photonics Rev.*, 2020, **15**, 2000410.
- 32 Q. Lin, Q. Wang, M. Liao, M. Xiong, X. Feng, X. Zhang, H. Dong, D. Zhu, F. Wu and Z. Mu, Trivalent chromium ions doped fluorides with both broad emission bandwidth and excellent luminescence thermal stability, *ACS Appl. Mater. Interfaces*, 2021, **13**, 18274-18282.